Shape, strain, and ordering of lateral InAs quantum dot molecules

B. Krause and T. H. Metzger

European Synchrotron Radiation Facility, Boîte Postale220, F-38043 Grenoble Cedex, France

A. Rastelli, R. Songmuang, S. Kiravittaya, and O. G. Schmidt

Max-Planck-Institut für Festkörperforschung, Heisenbergstrasse 1, D-70569 Stuttgart, Germany

The results of an x-ray study on freestanding, self-assembled InAs/GaAs quantum dots grown by molecular beam epitaxy are presented. The studied samples cover the range from statistically distributed single quantum dots to quantum dot bimolecules, and finally to quantum dot quadmolecules. The x-ray diffraction data of the single quantum dots and the bimolecules, obtained in grazing incidence geometry, have been analyzed using the isostrain model. An extended version of the isostrain model has been developed, including the lateral arrangement of the quantum dots within a quantum dot molecule and the superposition of the scattering from different parts of the dots. This model has been applied to the scattering maps of all three samples. Quantitative information about the positions of the dots, the shape, and the lattice parameter distribution of their crystalline core has been obtained. For the single dot and the bimolecule, a strong similarity of the shape and lattice parameter distribution has been found, in agreement with the similarity of their photoluminescence spectra.

PACS number(s): 68.65.Hb, 61.10.−i, 81.16.Rf, 81.16.Dn

I. INTRODUCTION

Semiconductor quantum dots have received much interest due to their unique structural and electronic properties.[1–6] They can be thought of as artificial atoms since their electrons are confined in three dimensions. In analogy to the natural hierarchy in a solid (from the single atom to the molecule, and finally to the crystal), the complexity of self-assembled quantum dot systems can be increased from single quantum dots to quantum dot molecules,[7–12] and finally to 3D quantum dot crystals.[13–17]

Quantum dot molecules are a special case of ordered quantum dots. They are closely placed groups of quantum dots, vertically[11,12] or laterally[7,8,10] arranged. The growth of these structures is motivated by the idea that they may act as a possible building block for quantum computers.

The electronic properties of a quantum dot are determined by shape, strain, and composition. X-ray scattering is a well-established tool to study the structural properties of free-standing and buried quantum dots.[15,17–20] However, depending on the studied quantum dot system, it can be very difficult to separate the influence of shape, position, and strain of the dots in the diffraction patterns.

In this paper, x-ray scattering is used to study freestanding, self-assembled InAs/GaAs quantum dots grown by molecular beam epitaxy. The samples are increasingly complex (see Fig. 1), ranging from statistically distributed single quantum dots over ordered and oriented arrangements of two quantum dots (bimolecules) up to ordered and oriented arrangements of four quantum dots (quadmolecules). It will be shown that the arrangement of the islands leads to additional interference effects in the diffracted intensity which are clearly distinct from the intensity distribution related to strain and shape of the dots.

Two methods are typically used for the analysis of the scattering of quantum dots: (1) the isostrain approach[21] and (2) finite element calculations.[18] The isostrain approach simplifies the lattice parameter distribution and the shape of the quantum dot (see Sec. III A). Within these simplifications, the shape of the dot and the height dependence of the laterally averaged lattice parameter are directly determined from the experimental data. In the finite element approach the shape and the concentration distribution within the quantum dot are assumed. The elastic strain field in the dot is determined. From this, the x-ray scattering of the object is calculated and compared and compared with the experimental data. Here, we will investigate the limits of the isostrain approach for quantum dot molecules and propose an extended model including the lateral arrangement of the quantum dots within a quantum dot molecule.

The structure of the paper is as follows. In Sec. II, the experimental details are given. Section III summarizes the methods used for the analysis of the data. The results of the x-ray experiments on single quantum dots, quantum dot bimolecules, and quadmolecules are presented in Sec. IV. They are analyzed in detail in Sec. V and Sec. VI contains the conclusions.

II. EXPERIMENTAL DETAILS

A. Sample preparation

Single, self-assembled InAs quantum dots on GaAs(001) are formed as a result of the lattice misfit between the GaAs
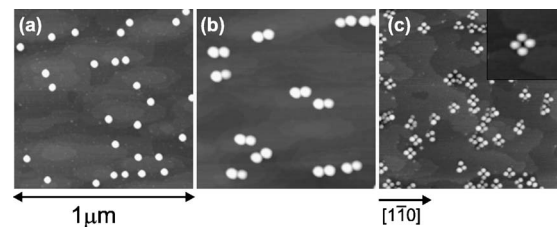
FIG. 1. AFM images from (a) conventional, single quantum dots, (b) bimolecules, and (c) quadmolecules. The inset in (c) shows an enlarged area of 0.1×0.1 μm^2.
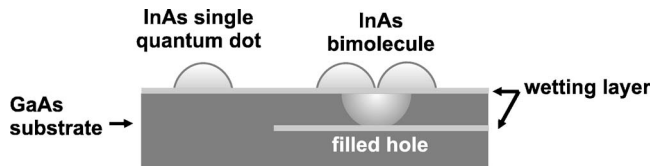
FIG. 2. Schematic showing the difference between a conventional quantum dot grown on a flat surface and a quantum dot molecule grown on top of the filled hole.

substrate with the lattice parameter a_{GaAs}=5.65 Å and the InAs film with a_{InAs}=6.06 Å. After the initial growth of a commensurate wetting layer, the total energy is minimized by forming 3D islands (Stranski-Krastanov growth).

Quantum dot molecules are produced in a more complex growth process,[8] consisting of several growth steps: (1) deposition of InAs quantum dots, (2) overgrowth of the InAs quantum dots by a GaAs cap layer, (3) selective etching of the overgrown quantum dots with $AsBr_3$, and (4) filling of the resulting holes with InAs and nucleation of quantum dot molecules on top of them. Figure 2 shows a schematic of a conventionally grown quantum dot and a quantum dot molecule.

For the dome-shaped[22] single quantum dots, shown in Fig. 1(a), 1.8 ML InAs have been deposited at 500 °C, forming quantum dots with a height of 120 Å and a diameter of 400 Å, as determined by noncontact atomic force microscopy (AFM) measurements. For the bimolecule sample [Fig. 1(b)], 50–60 Å deep holes produced by *in situ* etching have been overgrown by 2.5 ML InAs at a growth temperature of 500 °C. The bimolecules consist of two quantum dots of 170 Å height and a diameter of 500–600 Å, which are aligned in $[1\bar{1}0]$ direction. Their natural orientation in $[1\bar{1}0]$ direction has been further improved by the growth on a stepped surface with step edges parallel to $[1\bar{1}0]$. For the quadmolecules, shown in Fig. 1(c), the same holes have been overgrown by 1.6 ML InAs deposited at 450 °C. The dots have a height of about 40 Å, and a diameter of 200–300 Å. They are aligned in $[110]$ and $[1\bar{1}0]$ direction. Additionally, a sample consisting of holes filled with 1 ML InAs deposited at 500 °C has been studied. For this sample (in the following referred to as "filled holes") no surface corrugation has been detected in the AFM measurements. All samples have been deposited at low growth rates (0.01 ML/s), and show a density of about 3×10^9 objects/cm² of statistically distributed objects (objects can be quantum dots, quantum dot molecules, or filled holes, respectively). Since the samples have been exposed to air prior to the x-ray experiment, they are covered by natural oxide.

B. Experimental techniques

In order to study shape, ordering, and strain of the quantum dots, two x-ray scattering methods have been used: Grazing incidence x-ray diffraction (GID) and grazing incidence small-angle x-ray scattering (GISAXS). The methods are schematically shown in Fig. 3. Both methods are surface sensitive since the probing depth of the x rays can be limited
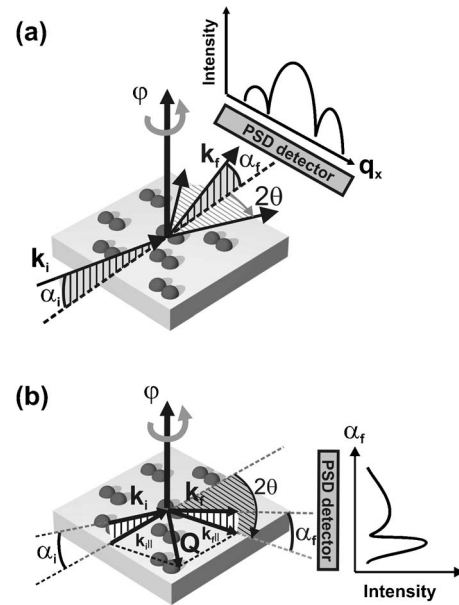
FIG. 3. Schematic of (a) grazing incidence small angle scattering (GISAXS) and (b) grazing incidence diffraction (GID) geometry.

by chosing a small incident angle α_i and exit angle α_f, i.e., α_i and α_f smaller than the critical angle of total external reflection α_c which equals 0.31° for GaAs at the x-ray energy 8 keV. Under these conditions, the probing depth of the x rays can be tuned from about 50 to several hundred Å.

In the GISAXS geometry [Fig. 3(a)], the scattering of the sample close to the forward direction is measured. The momentum transfer $\mathbf{Q}=\mathbf{k}_f-\mathbf{k}_i$, where $\mathbf{k}_i$ and $\mathbf{k}_f$ are the wave vectors of the incident and the scattered x-rays, respectively, is very small. Therefore, GISAXS is not sensitive to the crystalline structure. The measured x ray intensity is directly related to the Fourier transformation of the shape and the positional correlation of the quantum dots.

In GID geometry [Fig. 3(b)], the scattering angle 2θ and the momentum transfer are large, and the measured intensity is far away from the forward direction. The Bragg reflections of the lattice planes oriented perpendicular to the sample surface are measured, and information about lateral strain, shape, and position of the crystalline part of the quantum dots is obtained.

Typical GID measurements are radial and angular scans. In a radial scan, the direction of the momentum transfer $Q=Q_r$ relative to the in-plane lattice planes is kept constant and the intensity is measured at different Q_r. For this, the detector angle 2θ is increased between two data points by the angle $2\Delta\theta$, and the sample rotation angle φ around the surface normal is increased by $\Delta\theta$. In angular scans, the absolute value of Q is kept constant while its direction is changed by rotating the sample by $\Delta\varphi$ relative to the radial direction of the respective Bragg reflection. Q_r is calculated from

$$Q_r = \frac{4\pi}{\lambda} \sin\theta, \qquad (1)$$

where λ is the wave length of the x rays. For small $\Delta\varphi$, Q_a equals

$$Q_a = Q_r \sin(\Delta\varphi). \tag{2}$$

Further information about the measurement methods can be found, e.g., in Refs. 18 and 20.

The x-ray scattering experiments presented in this paper have been performed at the beamline ID01 of the European Synchrotron Radiation Facility (ESRF) in Grenoble, France. All measurements have been done at an x-ray energy $E = 8$ keV. During the measurements, the samples have been kept in He atmosphere to prevent further oxidation by the ozone produced by the intense x-ray beam.

For all experiments, a position sensitive detector (PSD) has been used. In GISAXS geometry, the detector has been mounted parallel to the sample surface [see Fig. 3(a)]. Lateral size and correlation of the quantum dots are visible along the PSD. In GID geometry, the detector has been mounted perpendicular to the sample surface in order to measure the α_f profile of the scattered intensity [see Fig. 3(b)]. In most of the GID measurements, reciprocal space maps (Q_r/Q_a maps) of the in-plane reflections have been recorded by measuring angular scans at different Q_r positions and integrating the intensity in α_f direction. For the analysis of the data using the isostrain model (see Sec. III A), line scans in Q_r and Q_a direction have been extracted from the maps.

III. DATA EVALUATION

A. Analysis of the GID data: Isostrain model

The isostrain method (shown schematically in Fig. 4) has been developed to directly determine the strain distribution of conventionally grown InAs quantum dots from GID data, without complex modeling.[21] It has been shown that the model works very nicely for systems which exhibit a large lattice parameter distribution.[21,23,24]

The basic idea of the method is the following. It is assumed that the lattice parameter of a coherently grown free-standing quantum dot varies monotonously from a small lattice parameter at the bottom of the quantum dot (i.e., a small lattice mismatch to the GaAs substrate) to large lattice parameters at the InAs rich top of the quantum dot (corresponding to a large lattice mismatch to the substrate). This leads to a continuous intensity distribution in reciprocal space, situated between the radial positions $Q_r = 2\pi/d_{GaAs}$ and $Q_r = 2\pi/d_{InAs}$ [Fig. 4(b)], where d is the respective lattice spacing. Each position Q_r corresponds to a slice of the quantum dot at the height z over the surface [Fig. 4(a)]. The radius of this slice with the lattice spacing $d(z) = 2\pi/Q_r$ is deduced from a fit of the intensity distribution in angular direction Q_a at the radial position Q_r. The scattering intensity $I(Q, r) = |F(Q, r)|^2$ is calculated using the form factor of a disk

$$F(Q, r) = \frac{2\pi r}{Q} J_1(rQ), \tag{3}$$

with the Bessel function $J_1(rQ)$ and the parameters $r = r(z)$ and $Q = Q_a$. At each Q_r, z can be determined from the position of the maximum in the α_f scan α_{max}.[21,25] The reason for
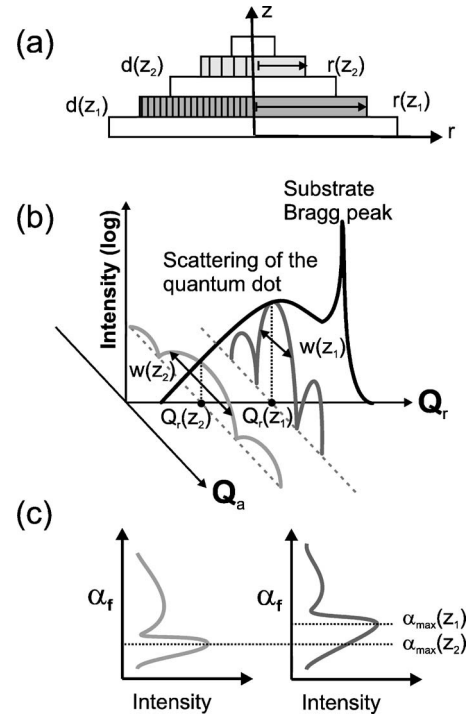
FIG. 4. Principle of the isostrain model. (a) The quantum dot is represented by a stack of disks. (b) The in-plane scattering of a quantum dot. To illustrate the model, the angular scattering of two disks at the heights z_1 and z_2 has been colorcoded. In (c), the respective α_f profiles are shown. For explanations see text.

the sensitivity of the α_f profile to the height of the slice is the following: Since the incident and scattered x-ray wave can also be reflected by the substrate surface, several scattering processes contribute to the x-ray intensity of a slice at the height z at a certain α_i and α_f (see Fig. 5): (1) the x rays are scattered by the slice, (2) the x rays are scattered by the slice and then reflected by the surface, (3) the x rays are first reflected by the surface and then scattered by the slice, and (4) the x rays are reflected by the surface, scattered by the slice, and then again reflected by the surface. The effective scattering amplitude F' of all four processes can be written as
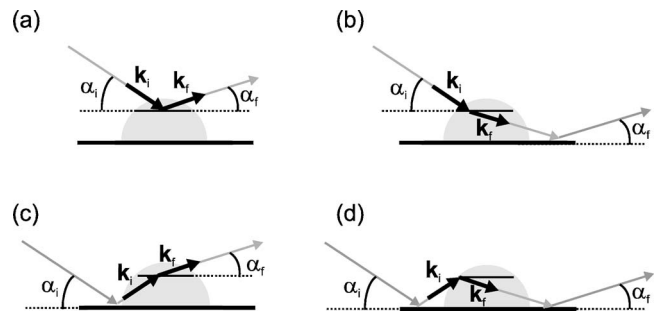
FIG. 5. Dominant scattering processes at a quantum dot on a substrate (for details see text).

$$F'(Q_a, r, z, \alpha_i, \alpha_f) = F(Q_a, r)e^{-2ik(\alpha_i+\alpha_f)z}t(\alpha_i, z)t(\alpha_f, z), \tag{4}$$

with the wave vector k, the form factor $F(Q_a,r)$ of a disk with the radius r at $Q=Q_a$ [Eq. (3)], and the effective transmittivity

$$t(\alpha, z) = 1 + R(\alpha)e^{-2ik\alpha z}. \tag{5}$$

α can be α_i or α_f, and $R(\alpha)$ is the Fresnel reflectivity. The scattered intensity $I(Q_a,r,z,\alpha_i,\alpha_f)$ is proportional to $|t(\alpha_i,z)|^2|t(\alpha_f,z)|^2$. At constant α_i, this function corresponds to the α_f profile. The first maximum of the α_f profile decreases with increasing z, following in good approximation the equation

$$z = \frac{1}{k\alpha_{\max}} \arccos \frac{\alpha_{\max}}{\alpha_c}, \tag{6}$$

with the wave vector k and the critical angle of total external reflection α_c.

B. Extension of the isostrain model

In order to include the lateral arrangement of the quantum dots within a quantum dot molecule and the superposition of the scattering from different disks, the isostrain model has been extended. Starting from the original model summarized above, each of the n quantum dots forming a quantum dot molecule ($n=1$ for the single quantum dot, $n=2$ for the bimolecule, and $n=4$ for the quadmolecule) is represented by a stack of disks. The disks are assumed to be circular, with a lattice spacing $d(z)$ and a radius $r(z)$. The scattering of disks at the same height, but situated in different dots, is added coherently, while the scattering of disks at different z is added incoherently. The total scattering intensity is

$$I(\mathbf{Q}) = \sum_z \left\langle \left| \sum_{j=1}^n F_j(r,d,\mathbf{q}) \right|^2 \right\rangle_{r(z),d(z)}, \tag{7}$$

with

$$F_j(r,d,\mathbf{q}) = f(\mathbf{Q})F(\mathbf{q},r)e^{-i\mathbf{Q}.\mathbf{R}_j}, \tag{8}$$

where $f(\mathbf{Q})$ is the scattering factor of the unit cell and $\mathbf{R}_j$ is the position of the disk belonging to the dot j. $F(\mathbf{q},r)$ is the form factor of the disk with the radius r, at $\mathbf{q}=\mathbf{Q}_d-\mathbf{Q}$, where $\mathbf{Q}_d$ is the Bragg peak position corresponding to the lattice spacing of the disk. For each z, the incoherent average over $r(z)$ and $d(z)$ is performed to take into account the size and lattice parameter distribution of the quantum dots. Equation (7) as been used for the simulation of the x-ray scattering of the single quantum dot (see Sec. V A). For the simulations, four scattering processes (see Fig. 5) have been taken into account[21] [for reasons of simplification not included in Eq. (7)]. In this paper, only the scattering of the strong (220) and ($2\bar{2}0$) reflection is discussed. The intensity distribution of these reflections is not very sensitive to the In concentration profile within the quantum dots as has been verified by some simulations including a compositional gradient within the quantum dot in z direction. Therefore, a compositional gradient has not been taken into account in the simulations presented here.

In x-ray diffraction experiments, the lattice parameter distribution of the dot ensemble is in competition with the correlation function of the dot-dot distance. For quantum dots with a wide lattice parameter distribution, even a size distribution of only few per cent can already be enough for losing the information about the lateral lateral arrangement of the dots within a quantum dot molecule. In this case, Eq. (7) reduces to

$$I(\mathbf{Q}) = n \sum_z \langle |F(r,d,\mathbf{q})|^2 \rangle_{r(z),d(z)}. \tag{9}$$

For $n=1$, this equation is identical to Eq. (7), i.e., to the scattering of a single quantum dot.

Depending on the island density, the shape and the lattice parameter distribution, a transition between the situations described in Eqs. (7) and (9) as a function of z is possible. This is described by

$$I(\mathbf{Q}) = \sum_z \left(c(z) \left\langle \left| \sum_{j=1}^n F(r,d,\mathbf{q}) \right|^2 \right\rangle_{r(z),d(z)} \right.$$
$$\left. + n[1 - c(z)]\langle |F(r,d,\mathbf{q})|^2 \rangle_{r(z),d(z)} \right), \tag{10}$$

where $0 \leq c(z) \leq 1$ is a weighting factor describing the (partial) correlation between the disks at the height z within one quantum dot molecule. This equation has been used for simulating the scattering of the bimolecules (see Sec. V B).

If the strain is small, as observed for the quadmolecules (see Sec. V C), all strain states superpose, and the height profile of the dots cannot be resolved. Equation (7) reduces to

$$I(\mathbf{Q}) = \left\langle \left| \sum_{j=1}^n F_j(r,d,\mathbf{q}) \right|^2 \right\rangle_{r,d}. \tag{11}$$

Here, the incoherent average is done over all lattice parameters and sizes within the quantum dot, independent of z.

C. Simulation of GISAXS data

The GISAXS intensity can be described by

$$I(\mathbf{Q}) \sim |F(\mathbf{Q})|^2 S(\mathbf{Q}), \tag{12}$$

where F is the form factor of a single object and S describes the spacial distribution of the objects, i.e., the correlation function of their positions. For the sample discussed here, the density of the objects (quantum dot bimolecules) is very low, and $S(\mathbf{q}) \approx 1$. The form factor can be calculated similarly to the GID measurements: each quantum dot is represented by a stack of disks, and the scattering of the different dots forming one molecule is coherently added. Since GISAXS is not sensitive to the lattice parameter distribution in the dots, the disks situated at different z can also be added coherently,
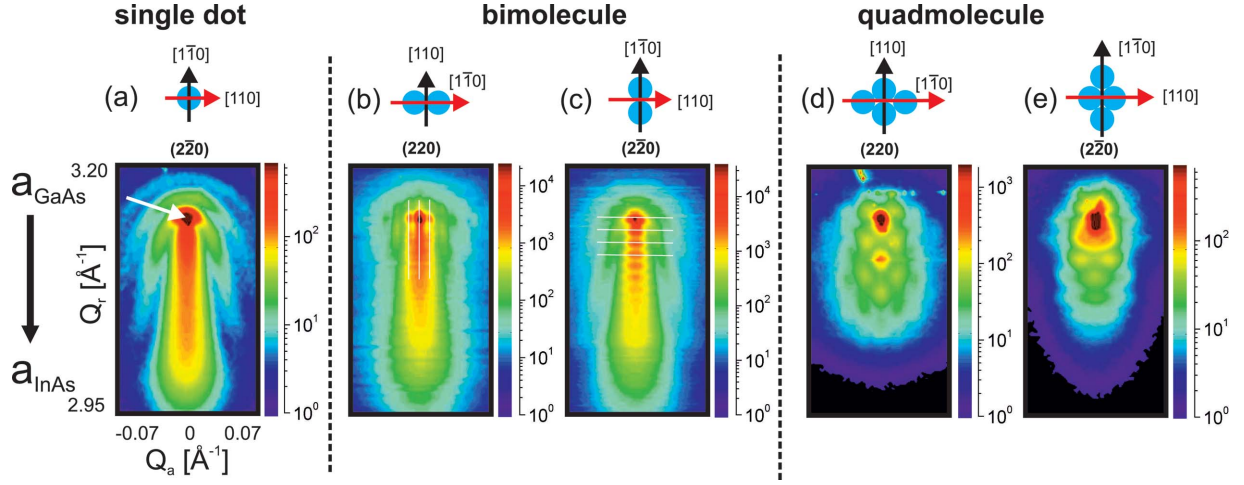
FIG. 6. (Color) In-plane scattering map of (a) the $(2\bar{2}0)$ reflection of the single quantum dot, (b) and (c) the (220) and the $(2\bar{2}0)$ reflection of the bimolecules, and (d) and (e) the (220) and the $(2\bar{2}0)$ reflection of the quadmolecules. The range Q_r in radial direction and Q_a in angular direction, indicated in (a), are the same for all images. The intensity is plotted logarithmically (arb. units), values below the range of the color scale are plotted in black, values above in dark red. On top of each figure, a schematic of the quantum dot arrangement is shown, with a red arrow indicating the direction of Q_a, and a black arrow indicating the direction of Q_r. The white arrow in (a) indicates the position of the GaAs substrate Bragg peak. In (b) and (c), the oscillations due to the ordering of the quantum dots are highlighted by white lines.

$$I(\mathbf{Q}) = \left| \sum_z \left\langle \sum_{j=1}^n F_j(r,\mathbf{Q}) \right\rangle_{r(z)} \right|^2, \qquad (13)$$

with

$$F_j(r,\mathbf{Q}) = F(r,\mathbf{Q})e^{i\mathbf{R}_j \cdot \mathbf{Q}}. \qquad (14)$$

For the simulations presented in Sec. V B, four scattering processes (see Fig. 5) have been taken into account.[25]

IV. RESULTS

A. GID Q_r/Q_a maps

Figure 6(a) shows measured Q_r/Q_a in-plane scattering map close to the $(2\bar{2}0)$ reflection of the single dot, Figs. 6(b) and 6(c) the maps of the (220) and the $(2\bar{2}0)$ reflection of the bimolecule, and Figs. 6(d) and 6(e) the maps of the (220) and the $(2\bar{2}0)$ reflection of the quadmolecule. The radial direction Q_r is mainly sensitive to the lattice parameter distribution, and the angular direction Q_a is sensitive to the shape of the objects. The measurements of the single dot and the quadmolecule have been performed at $\alpha_i = 0.2°$, the measurements of the bimolecule at $\alpha_i = 0.25°$. For all data shown, the intensity has been integrated over α_f.

The Q_r/Q_a maps show a relatively broad peak around the narrow substrate Bragg peak (due to the colorscale, the substrate bragg peak itself is not visible in the maps). This peak is related to the strained substrate below the quantum dot and to the GaAs rich lower part of the quantum dot. It is continued by an intensity distribution elongated in Q_r. For the single quantum dot, the central hump of the intensity distribution is unstructured. For the bimolecule and the quadmolecule, additional features are visible. The (220) map of the bimolecule shows stripes in radial direction, the $(2\bar{2}0)$ map

in angular direction. This is due to the alignment of the dots in $[1\bar{1}0]$, which for (220) is the angular direction and for $(2\bar{2}0)$ is the radial direction. The stripes visible in (220) are washed out at lower Q_r. The central hump of both the (220) and the $(2\bar{2}0)$ reflection of the quadmolecule is modulated by broad peaks instead of stripes, due to the alignment of the dots in two directions. The peak positions of (220) and $(2\bar{2}0)$ are not identical, indicating that the distances between the dots are different in [110] and $[1\bar{1}0]$ direction.

The elongated shape of the intensity distribution is related to the lattice parameter distribution in the quantum dot between a_{InAs} and a_{GaAs}. The measurements for the bimolecule and the single dot look very similar, the width of the central hump in angular direction increasing with decreasing Q_r. The InAs content of the quantum dot increases with increasing height z, i.e., the lattice parameter increases (corresponding to a smaller Q_r), while the size of the quantum dot decreases (corresponding to a broadening of the peak in angular direction). For the quadmolecule, the width of the central hump is independend of Q_r, indicating a superposition of the different strain states which might be related to the small height of the quantum dots.

For the single dot and the bimolecule, intensity bands curved around the substrate Bragg position are observed, continuing parallel to the central hump. These features are also related to the size of the quantum dot. In an angular scan at a certain Q_r, they show up as oscillations around the central peak. The damping of the oscillations is a measure for the size distribution of the disks with a certain lattice parameter. The oscillations in Q_a visible for the bimolecule are much less pronounced than the respective oscillations observed for the single dot. This indicates that the size distribution of the quantum dots forming the bimolecule is larger than the very narrow size distribution of the single quantum dot.
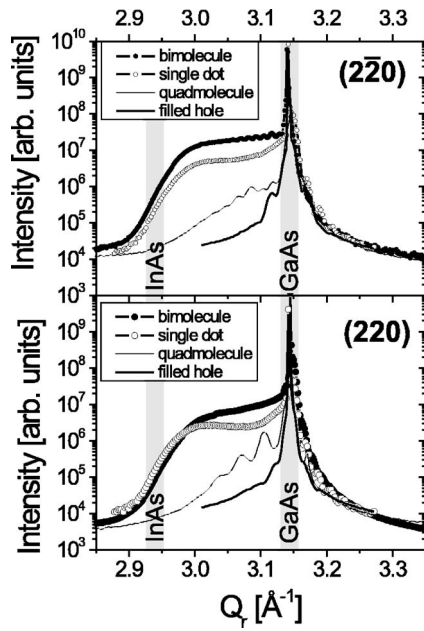
FIG. 7. Comparison of the (220) and (2$\bar{2}$0) radial scans for the single dot, the bimolecule, the quadmolecule, and the "filled hole" sample. The positions of the relaxed GaAs and InAs Bragg peak are indicated.

B. GID radial scans

A radial scan is a cut of the reciprocal space maps along Q_r, at $Q_a=0$. In addition to the single dot, the bimolecule, and the quadmolecule ($\alpha_i=0.2°$), also a sample with filled holes has been studied ($\alpha_i=0.24°$). Figure 7 shows the radial scan of the samples in [110] and [1$\bar{1}$0] direction, with the measured intensity integrated over α_f. In all cases, α_i is kept below the critical angle of total external reflection, α_c =0.31°, corresponding to a penetration depth of the evanescent x-ray wave of about 60 Å.

All measurements show a peak close to the substrate Bragg position induced by the strain in the substrate, and in the case of the dots also due to the scattering of the lower part of the dots. The conventional quantum dots and the bimolecules show a similar intensity distribution, with a maximum near the GaAs substrate peak and a broad shoulder towards the position of the relaxed InAs. For the quadmolecule, this shoulder is less pronounced and less extended in Q_r direction, indicating that the lattice parameter distribution of the quadmolecule is shifted in direction of a_{GaAs}. As already observed in the Q_r/Q_a maps (Fig. 6), due to the alignment of the dots the intensity distributions along [1$\bar{1}$0] and [110] direction of the bimolecule and the quadmolecule are not equivalent.

The scattering of the "filled hole" sample is restricted to the area around the substrate peak, and only a slight asymmetry is visible. This result is important for the qualitative understanding of the scattering of the quantum dot molecules. While the scattering around the substrate Bragg peak cannot be attributed unambiguously to either the dot-induced strain in the substrate, the influence of the filled hole, or to the quantum dots itself, the scattering at lower Q_r is clearly related to the quantum dots. The average lattice parameter of the "filled hole" sample is close to a_{GaAs}. This can have two reasons: (1) the In$_x$Ga$_{1-x}$As in the hole cannot relax laterally due to the confinement by the surrounding GaAs matrix and (2) the Ga concentration in the hole is relatively high due to surface diffusion of GaAs during the deposition of InAs.

C. GID Q_r/α_f maps

Figure 8(a) shows the α_f profile, i.e., $|t(\alpha_i,z)|^2|t(\alpha_f,z)|^2$ at a constant α_i (see Sec. III A), as a function of the height z of a quantum dot slice over the substrate surface, calculated for $\alpha_i=0.2°$. For material at $z\leqslant 0$, the first intensity maximum is at α_c, for $z>0$ it shifts to lower values. The position of the first intensity maximum is given by Eq. (6). Figures 8(b)–8(e) show α_f spectra measured at each point of a (2$\bar{2}$0) radial scan, for (b) the single dot, (c) the bimolecule, (d) the quadmolecule, and (e) the "filled hole" sample. For the single quantum dot and the bimolecule, the position of the maximum in the α_f profile shifts with decreasing Q_r to values lower than the critical angle. The calculation shown in
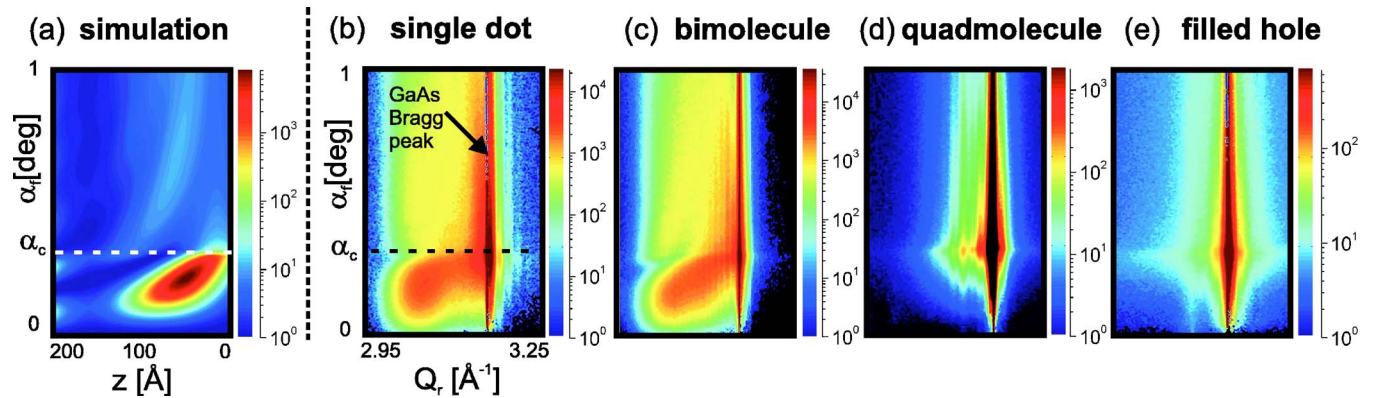
FIG. 8. (Color online) (a) α_f profile as a function of the height z of a quantum dot slice, calculated for $\alpha_i=0.2°$. (b)–(e) α_f spectrum at each point of a radial scan through the (2$\bar{2}$0) reflection, for (b) the single dot, (c) the bimolecule, and (d) the quadmolecule at $\alpha_i=0.2°$, and for (e) the "filled hole" sample at $\alpha_i=0.24°$. The range of Q_r and of α_f, indicated in (b), is the same for all images. The intensity is plotted logarithmically (arb. units), values below the range of the color scale are plotted in black, values above in dark red.
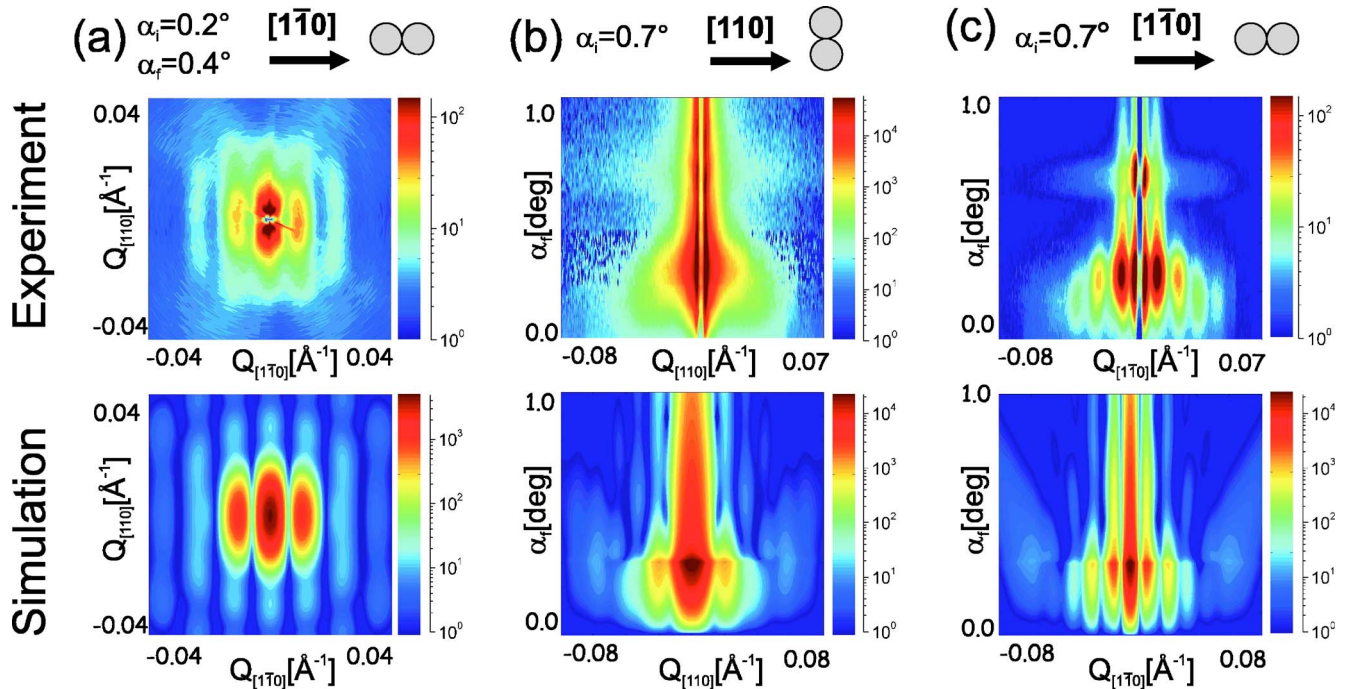
FIG. 9. (Color online) GISAXS measurements of the quantum dot bimolecules and their simulations, shown in logarithmic intensity scale (arb. units, values below the range of the color scale are plotted in blue, values above in dark red). 2D intensity distribution at (a) constant incident angle α_i and exit angle α_f, (b) constant α_i and variable α_f with the in plane scattering vector perpendicular to the molecular axis, and (c) constant α_i and variable α_f with the in plane scattering vector parallel to the molecular axis. The scanning direction relative to the orientation of the bimolecule is indicated.

Fig. 8(a) and the map of the single dot and the bimolecule are very similar since the laterally averaged lattice parameter increases monotonously with z. The Q_r range of the radial scans for the single dot and the bimolecule is the same, while the shape of the first maximum of the a_f profile is different. This indicates that the bimolecule and the single dot have a similar lattice parameter distribution, but a certain lattice parameter is located at different z in the respective samples.

For the quadmolecule and the "filled hole" sample, no shift of α_f has been observed. This is expected for the "filled hole" sample, but not for the quadmolecules. The AFM measurements of the "filled hole" sample show a completely flat surface consistent with the x-ray observation. The AFM measurements of the quadmolecule show quantum dots with a height of about 40 Å. According to Fig. 8(a), a shift of the first maximum would be expected.

D. GISAXS on bimolecule

Figure 9(a) shows a GISAXS map of the bimolecules, measured with the PSD parallel to the sample surface at fixed incident angle $\alpha_i=0.2°$ and exit angle $\alpha_f=0.4°$ while rotating the sample around the surface normal. Figures 9(b) and 9(c) show α_f maps in the [110] and [1$\bar{1}$0] direction, the two lateral symmetry axis of the bimolecules. These maps correspond to cuts at $Q_{[110]}=0$ and $Q_{[1\bar{1}0]}=0$ perpendicular to the intensity distribution shown in Fig. 9(a), measured at different α_f.

Figure 9(a) shows the intensity distribution expected for a single quantum dot, superposed by stripes along the [110]

direction. The shape of a single dot leads to an approximately circular intensity distribution. Slight deviations from the circular shape are related to the fact that the actual shape of the dot is not circular but slightly elongated and faceted with steep {011} and {111} and shallow {137} facets.[22] The signature of the ordering of the dots is the stripe pattern. It indicates that the dot pairs are predominantly aligned in the in [1$\bar{1}$0] direction.

Figure 9(b) shows the α_f map in [110] direction where only the form factor of the single dot is visible. Figure 9(c) shows the α_f map in [1$\bar{1}$0] direction, where the oscillations corresponding to the size of the single dot are superposed by oscillations due to the ordering. The intensity increase around $\alpha_f=\alpha_i=0.7°$ is due to the diffuse scattering of the reflected x-ray beam.

V. DISCUSSION

A. Single quantum dot

From the Q_r/Q_a map shown in Fig. 6(a), and the Q_r/α_f map shown in Fig. 8(b), the shape and the laterally averaged lattice constant distribution of the single quantum dot as a function of z have been determined using the isostrain method. Figures 10 and 11 summarize the results.

The height z of the isostrain slice normalized to the maximum height $z_{max}=75$ Å, and the radius r of the isostrain slice are shown in Figs. 10(a) and 10(b) as a function of the lattice parameter. Both r and z vary linearly over a wide range of a.
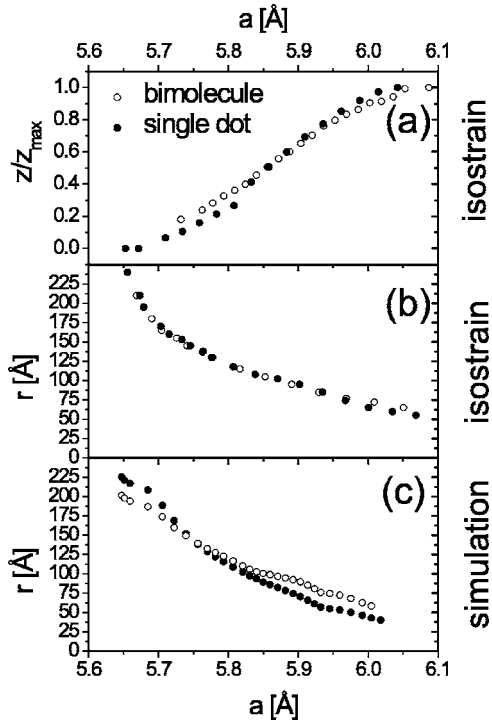
FIG. 10. (a) Isostrain result for the height as a function of the lattice parameter, (b) isostrain result for the radius as a function of the lattice parameter, and (c) radius as a function of the lattice parameter as result of the extended model.

FIG. 11. Comparison between isostrain result and result of the extended model for (a) the single quantum dot, and (b) the bimolecule. (c) Dot shape for the conventional quantum dots and the bimolecule as derived from the extended model.

From $r(a)$ and $z(a)$, the shape $r(z)$ of the quantum dot has been derived, plotted in Fig. 11(a).

The radius of the dot decreases with increasing height, and it seems that a smaller upper part of the quantum dot sits on top of a wider socket with a height of about 25 Å. The lattice parameter varies between a_{GaAs} at the bottom of the quantum dot and a_{InAs} at the top of the quantum dot.

The results of the isostrain model have been used as input for the extended model, using Eq. (7). Q_r/Q_a maps and Q_r/α_f maps have been calculated, and the input parameters have been refined iteratively. Figure 12(a) shows the calculated Q_r/Q_a map. It reproduces the main features of the experimental map shown in Fig. 6(a), including the peak around the substrate Bragg peak position, the curved intensity bands around the Bragg peak, and the shape of the elongated intensity distribution related to the size and the lattice parameter distribution of the dot. The calculated Q_r/α_f map is shown in Fig. 12(d). The general shape of the intensity distribution, i.e., the elongated intensity bump below α_c and shape of the the weak intensity distribution above α_c, is well reproduced. The parameters used for the simulation are summarized in Fig. 10(c), showing $r(a)$, and Fig. 11(c), showing the shape of the dot. Figure 11(a) compares the shape determined by the isostrain model with the result of the simulations.

Within small deviations, the shape and the lattice parameter distribution of the dot are comparable to the result of the isostrain model. The size distribution of the radius [indicated by the error bars in Fig. 11(c)] varies between 4 and 7 % of $r(z)$, corresponding to absolute variations of 4 to 10 Å.

B. Bimolecule

From the Q_r/Q_a map shown in Figs. 6(b) and 6(c), and the Q_r/α_f map shown in Fig. 8(c), the shape and the laterally averaged lattice constant distribution of the quantum dots forming the bimolecule have been determined by the isostrain method. $z(a)/z_{max}$ is shown in Figs. 10(a), $r(a)$ in Fig. 10(b), and the resulting shape $r(z)$ in Fig. 11(b). $r(d)$ and $z(d)/z_{max}$ are very similar to the values found for the single dot. The main difference is that the maximum height z_{max} =137 Å of the bimolecule is nearly double the height of the single dot. The dot shape is not a perfect truncated cone, but a smaller upper part on top of a wider socket with a radius of 250 Å and a height of about 30–40 Å.

As for the single dot, the results of the isostrain approach have been used as input parameters for the extended model. Several simulations, assuming coherent and incoherent addition of the scattering of the dots forming the bimolecule have been tested. It has been found that a transition between coherent and incoherent addition as a function of z [see Eq. (10)] is necessary to reproduce all experimentally observed features. The scattering of the lower part of the dots (more exactly of the strain field below the dot and the socket of the dot with $d \approx d_{GaAs}$ since both contributions cannot be separated experimentally) is added coherently, the scattering of the upper part of the dots with $d > d_{GaAs}$ is added incoherently. In the simulations, this has been taken into account by setting the ration of coherently added disks, i.e., $c(z)$ in Eq. (10), as follows: $c(z)=1$ for $z \leqslant 10$ Å, $c(z)=0$ for $z \geqslant 45$ Å, and $c(z)$ varying linearly between 1 and 0 for 10 Å$< z$
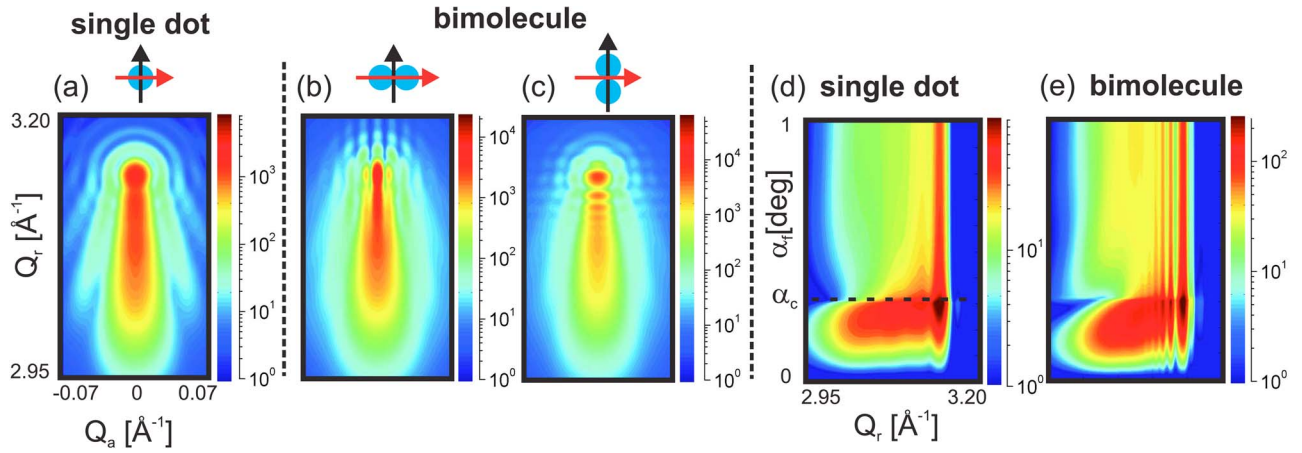
FIG. 12. (Color online) Simulation of the in-plane Q_r/Q_a maps and the Q_r/α_f maps of the bimolecule and the single quantum dot sample. Q_r/Q_a maps: (a) (220) reflection of the single quantum dot, (b) (220) reflection of the bimolecules, and (c) ($2\bar{2}0$) reflection of the bimolecules [plotrange indicated in (a)]. On top of each figure, a schematic of the quantum dot arrangement is shown. The red arrow indicates the direction of Q_a, the black arrow the direction of Q_r. Q_r/α_f maps: (d) ($2\bar{2}0$) reflection of the single dot and (e) ($2\bar{2}0$) reflection of the bimolecule [plot range indicated in (d)]. The intensity is plotted logarithmically (arb. units), values below the range of the color scale are plotted in blue, values above in dark red.

< 45 Å. This corresponds to a transition from coherent to incoherent addition of the neighbouring dots within the socket of the quantum dots.

The two dots forming the bimolecule are found to touch each other. Figures 12(b) and 12(c) show the calculated Q_r and Q_a maps of the (220) and ($2\bar{2}0$) reflection of the bimolecule. In addition to the general shape of the intensity distribution, the intensity oscillations due to the ordering of the dots are reproduced. As in the experimental data, for (220) the vertical stripes are pronounced around the substrate Bragg peak and damped at lower Q_r.

Figure 12(e) shows the calculated α_f map which reproduces well the tilted intensity bump observed below α_c, and the shape of the intensity distribution above α_c. The refined parameters are summarized in Fig. 10(c) (radius of the disk as a function of the lattice parameter) and Fig. 11(c) (shape of the dot). Compared to the shape deduced from the isostrain model, the upper part of the dot is about 20% smaller. The size distribution of the disks varies between 7% at the bottom and 25% at the top of the dot, the absolute variations are between 15 and 25 Å.

The shape of the quantum dot has also been determined from the GISAXS data. For the form factor of the bimolecule, the following model has been used: one dot is represented by a truncated cone with the lower radius r_1, the upper radius r_2, and the height h (see Fig. 13). The two dots forming the quantum dot molecule are assumed to touch each other and to be perfectly aligned in $[1\bar{1}0]$ direction. The best agreement of the simulations with the experimental data has been found using the parameters $r_1 = 260 \pm 20$ Å, $r_2 = 35 \pm 35$ Å, $h = 170 \pm 20$ Å, and a size distribution of 8%. The simulations are shown in Fig. 9. Further simulations, using more complex models varying the orientation, the shape, and the distance between the dots have been carried out. Within the experimental error, these simulations confirmed the simple model. This indicates that the self-organized bimol-

ecule sample is very homogenous and that the orientational distribution is very narrow, of the order of a few degrees over the entire sample.

Figure 14 compares the average shape of the quantum dots as derived by the GISAXS data with the shape determined from the simulations of the GID data. The height of the quantum dot observed by GISAXS is about 30 Å larger than the height determined by GID. Within the experimental error, the radius of the socket of the dot is comparable to the AFM result, and the radius of the upper part is is about 50 Å larger than obtained from GISAXS/AFM.

C. Quadmolecule

The precondition for the isostrain model are a sufficient ratio between the size and the lattice parameter distribution within the quantum dot. This is not fulfilled for the quadmolecule. Instead of the height profile of the size and strain, only values averaged over the object height can be determined. In Fig. 15, the Q_r/Q_a maps of the (220) and ($2\bar{2}0$) reflection are shown. The positions of the peaks related to the lateral ar-
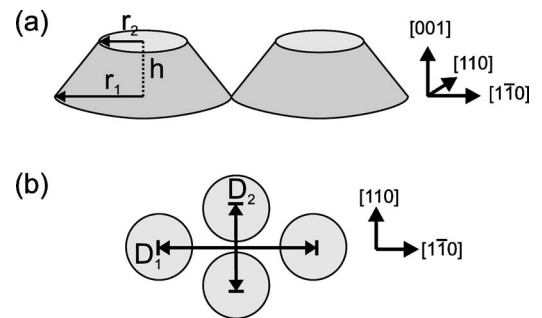
FIG. 13. Schematic of the model used for (a) the GISAXS data of the bimolecule and (b) the analysis of the GID data for the quadmolecule.
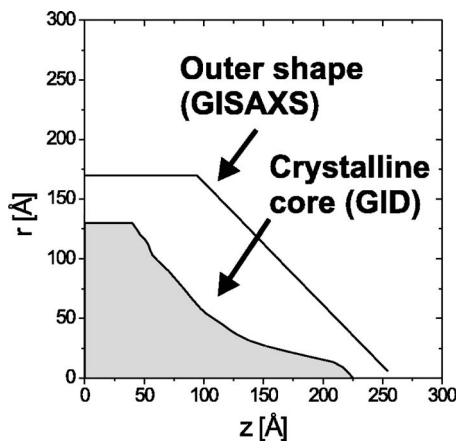
FIG. 14. Comparison of the outer dot shape as derived from GISAXS with the shape of the crystalline core determined from the simulation of the GID data.

rangement of the quantum dots within a molecule are marked by circles. They form a rhombohedral 2D lattice which for the (220) reflection is turned by 90° relative to the lattice of the (2$\bar{2}$0) reflection. In both cases, one of the peaks coincides with the peak at the substrate Bragg peak position, i.e., the average lattice constant of the quantum dots is close to d_{GaAs}. Based on this observation, the following model has been assumed [see Fig. 13(b)]: the quantum dots forming the quadmolecule are circular with the average radius $\langle r \rangle$, and the average lattice constant $\langle a \rangle$. Two dots are aligned in [1$\bar{1}$0] direction with the distance D_1, and two aligned in [110] direction with the distance D_2.

Using Eq. (11), the Q_r/Q_a maps of the (220) and the (2$\bar{2}$0) reflection have been calculated (see Fig. 15). The pa-
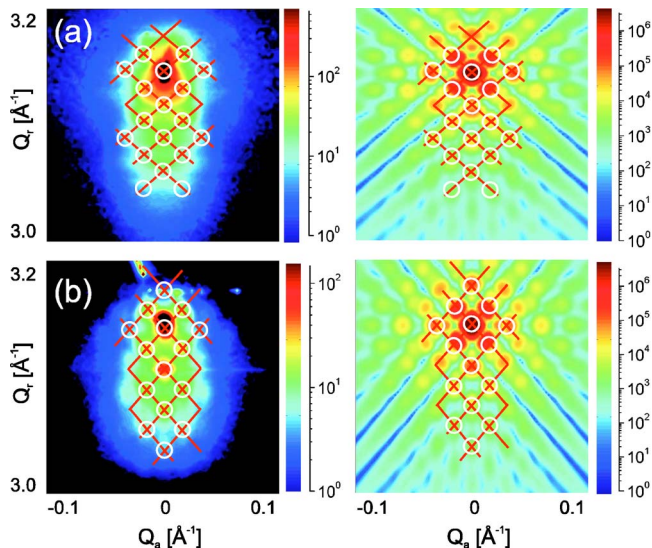
FIG. 15. (Color online) Direct comparison between GID experiment and simulation of the quadmolecule sample, showing the in-plane scattering map of (a) the [2$\bar{2}$0] reflection and (b) the [220] reflection. The peak positions are indicated in the respective the experimental (left side) and calculated maps (right side). The intensity is plotted logarithmically (arb. units), values below the range of the color scale are plotted in black, values above in dark red.

rameters $D_1 = 420$ Å, $D_2 = 360$ Å, $r = 140$ Å, $\langle d \rangle = 6.563$ Å, and a size distribution of 10%, have been used. For better comparison, the pattern indicating the peak positions of the experimental data has been superposed to the simulations. The simulations explain the peak positions but not the lattice parameter distribution in the dots composing the quadmolecule, since they take into account an average lattice parameter. An error of about 20 Å for the distance of the quantum dots, and an error of 10 Å for the radius of the quantum dots has been estimated using different parameter sets.

D. Comparison of the different samples

Within the experimental error, the diameter at the foot of the crystalline core determined for the single dot and the bimolecule, as well as the average diameter observed for the quadmolecule, agrees with the diameter observed for the individual quantum dots by AFM.

The bimolecules and the quadmolecules are well aligned along the substrate [1$\bar{1}$0] direction. The quantum dots forming the bimolecule touch in [1$\bar{1}$0] direction, for the average quadmolecule, the dots do not touch in [110] and [1$\bar{1}$0] direction but along directions close to [100] and [010]. For the quadmolecule, the [110] and [1$\bar{1}$0] directions are not equivalent. The dots are further apart from each other in [1$\bar{1}$0] direction, which is the direction with the higher surface diffusion coefficient.[26] In contrast to this, the extension of the filled hole is larger in [110] direction than in [1$\bar{1}$0] direction.[8] It shows that the nucleation places for the quantum dots forming the quadmolecule are not simply the borders of the initial hole, but that the nucleation mechanism is more complicated.

Within the experimental error, in all cases the scattering of the dots could be modeled using circular disks. No significant in-plane anisotropy in the shape of the dots was observed. An anisotropy larger than 10–20 Å would show clearly in an inequivalence of the laue oscillations around the substrate Bragg peak in [110] and [1$\bar{1}$0] direction which has not been found.

For the single quantum dots, but even more for the bimolecule, differences between the isostrain results and the refined parameters used for the simulations have been found [see Figs. 11(a) and 11(b)]. For the radius of the bimolecule, the results differ by up to about 20 Å. The lattice parameter on top of the quantum dot found in the simulations is slightly smaller than the isostrain result, while the normalized z is the same for both methods. The observed differences can be explained by a systematic error of the isostrain model. The radius is underestimated since the overlap of the scattering of different disks in radial direction is not taken into account.

In the extended model, the scattering of different dots forming one molecule has been added coherently only for $a \approx a_{GaAs}$. For the quadmolecule, this corresponds to the strain field below the dot and the average dot, for the bimolecule this corresponds to the strain field below the dot and the socket of the dot. For the single dot and the bimolecule, where the z profile of the dot could be resolved, the scatter-

ing of slices located at different z has been added incoherently.

The quantum dot dots on all samples have a narrow size distribution, and the dot molecules are well aligned with respect to the substrate and show a narrow positional distribution. The reason for the transition between coherent and incoherent addition of the scattering is the high sensitivity of the x-ray diffraction method to even a narrow size distribution of about a few per cent, if it is applied to samples with a large lattice parameter distribution, The strain field and the socket of the dot include a large amount of material with a similar lattice parameter. In contrast to this, each strain state with $a > a_{GaAs}$ corresponds to a very small amount of material, which in each dot is situated at a slightly different height, with a slightly different radius. In the first case, due to the large amount of material contributing to the scattering of each dot molecule at the same Q_r, the ordering of the dots is visible in the x-ray diffraction pattern. In the second case, the information about the ordering of the dots is lost.

For the bimolecule, a difference between the outer shape and height (as determined by GISAXS, in agreement with the AFM observations), and the shape and height of the crystalline core (determined by GID) has been observed. For the single dot and the quadmolecule sample, the crystalline core of one dot is also about 30 Å smaller than expected from the AFM results. It is important to note that for the quadmolecules, the AFM height is about 40 Å, while by x-ray diffraction no height could be resolved due to the small height of the dots and the narrow strain distribution.

For all samples, the difference between the outer shape and the size of the crystalline core can be explained by the formation of about 30 Å of natural oxide. The samples have been exposed to air before the measurements, and an amorphous oxide layer would not be visible in the GID measurements. It has been found that the thickness of the natural oxide of GaAs wafers reaches a thickness of about 20–30 Å after long-time air exposition.[27,28] The oxidation process is expected to reduce the size of the crystalline core of the dots by an even larger amount since InAs is known to oxidize faster than GaAs.[29]

Figure 16 shows a sketch of how the oxidation might modify the shape of a quantum dot. The oxidation can explain the smaller crystalline size and the socket of the quantum dot. In the case of the quadmolecule, the small dots are nearly completely oxidized, and the observed scattering originates mainly from the strain field within the substrate and the crystalline socket. For the bimolecule and the single dot, a large part of the scattering (especially the part sensitive to the alignment of the dots) is due to the strain field below the dots and the GaAs socket of the dots.

One important aspect of the oxidation is that the measured lattice parameter distribution of an oxidized dot is not identical to the lattice parameter distribution of the initial dot. The amount of crystalline material with lattice parameters close to a_{InAs} is reduced by the oxidation.
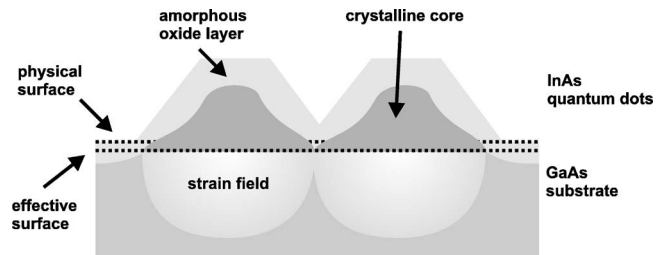
FIG. 16. Schematic of the model for the quantum dots consistent with the AFM, the GISAXS, and the x-ray diffraction results.

VI. CONCLUSIONS

We have presented the results of grazing incidence x-ray scattering experiments (GID and GISAXS) on single quantum dots, quantum dot bimolecules, and quadmolecules. Additionally, a precursor state of the quantum dot molecules, a hole in a GaAs substrate filled with a mixture of GaAs and InAs, has been investigated for comparison.

The scattering of the "filled hole" sample is located around the substrate Bragg peak, similar to the strain field below a conventional quantum dot. Therefore, the scattering of both the single quantum dot and the quantum dot molecules can be analyzed in the same way.

For the analysis of the data, two models have been used: the original isostrain model,[21] and an extended version including the ordering of the dots and the superposition of different strain states. The directional alignment and the correlation of the positions of the quantum dots forming a molecule have been observed, and their average position within the molecule has been determined. From the GID data, information about the shape and the lattice parameter distribution of the crystalline core of the quantum dots has been derived. The size of the quantum dots observed by GISAXS and AFM differs from the size of the crystalline core determined from the GID measurements. This can be explained by a partial amorphization of the dots due to the natural oxide formed at their surface.

The similarity between the photoluminescence (PL) spectra of the single quantum dot and the bimolecule is very intriguing.[8] The PL is strongly related to the shape, the strain, and the interdiffusion in the quantum dot. The here presented results confirm the similarity between the shape and the lattice parameter distribution of both samples.

[1] P. Michler, A. Kiraz, C. Becher, W. V. Schoenfeld, P. M. Petroff, L. Zhang, E. Hu, and A. Imamoglu, Science **290**, 2282 (2000).

[2] A. Zrenner, E. Beham, S. Stufler, F. Findeis, M. Bichler, and G. Abstreiter, Nature (London) **418**, 612 (2002).

[3] K. Karrai, R. J. Warburton, C. Schulhauser, A. Högele, B. Urbaszek, E. J. McGhee, A. O. Govorov, J. M. Garcia, B. D. Gerardot, and P. M. Petroff, Nature (London) **427**, 135 (2004).

[4] M. Kroutvar, Y. Ducommun, D. Heiss, M. Bichler, D. Schuh, G. Abstreiter, and J. J. Finley, Nature (London) **432**, 81 (2004).

[5] J. P. Reithmaier, G. Sek, A. Löffler, C. Hofmann, S. Kuhn, S. Reitzenstein, L. V. Keldysh, V. D. Kulakovskii, T. L. Reinecke, and A. Forchel, Nature (London) **432**, 197 (2004).

[6] T. Yoshie, A. Scherer, J. Hendrickson, G. Khitrova, H. M. Gibbs, G. Rupper, C. Ell, O. B. Shchekin, and D. G. Deppe, Nature (London) **432**, 200 (2004).

[7] O. G. Schmidt, C. Deneke, S. Kiravittaya, R. Songmuang, H. Heidemeyer, Y. Nakamura, R. Zapf-Gottwick, C. Müller, and N. Y. Jin-Phillipp, IEEE J. Sel. Top. Quantum Electron. **8**, 1025 (2002).

[8] R. Songmuang, S. Kiravittaya, and O. G. Schmidt, Appl. Phys. Lett. **82**, 2892 (2003).

[9] S. Kiravittaya, R. Songmuang, N. Y. Jin-Phillipp, S. Panayakeow, and O. G. Schmidt, J. Cryst. Growth **251**, 258 (2003).

[10] T. v. Lippen, R. Nötzel, G. J. Hamhuis, and J. H. Wolter, Appl. Phys. Lett. **85**, 118 (2004).

[11] I. Shtrichman, C. Metzner, B. D. Gerardot, W. V. Schoenfeld, and P. M. Petroff, Phys. Rev. B **65**, 081303(R) (2002).

[12] H. J. Krenner, M. Sabathil, E. C. Clark, A. Kress, D. Schuh, M. Bichler, G. Abstreiter, and J. J. Finley, Phys. Rev. Lett. **94**, 057402 (2005).

[13] S. Kiravittaya, H. Heidemeyer, and O. G. Schmidt, Physica E (Amsterdam) **23**, 253 (2004).

[14] H. Heidemeyer, C. Müller, and O. G. Schmidt, Physica E (Amsterdam) **23**, 237 (2004).

[15] G. Springholz, V. Holy, M. Pinczolits, and G. Bauer, Science **282**, 734 (1998).

[16] O. G. Schmidt *et al.* Surf. Sci. **514**, 10 (2002).

[17] J. Stangl, V. Holý, and G. Bauer, Rev. Mod. Phys. **76**, 725 (2004).

[18] M. Schmidbauer, M. Hanke, and R. Köhler, Cryst. Res. Technol. **37**, 3 (1998).

[19] H. Renevier, M. G. Proietti, S. Grenier, C. Ciatto, L. González, J. M. García, J. M. Gérard, and J. García, Mater. Sci. Eng., B **101**, 174 (2003).

[20] U. Pietsch, V. Holý, and T. Baumbach, *High-resolution X-ray Scattering from Thin Films and Lateral Nanostructures* (Springer-Verlag, Berlin, 2004).

[21] I. Kegel, T. H. Metzger, A. Lorke, J. Peisl, J. Stangl, G. Bauer, K. Nordlund, W. V. Schoenfeld, and P. M. Petroff, Phys. Rev. B **63**, 035318 (2001).

[22] G. Costantini, A. Rastelli, C. Manzano, R. Songmuang, O. G. Schmidt, K. Kern, and H. von Känel, Appl. Phys. Lett. **85**, 5673 (2004).

[23] C.-H. Hsu, H.-Y. Lee, Y.-W. Hsieh, Y. Stetsko, M.-T. Tang, K. Liang, N. Yeh, J.-I. Chyi, and D. Noh, Physica B **336**, 98 (2003).

[24] A. Malachias, W. N. R. M. V. B. Moreira, S. Kycia, and R. Magalhaes-Paniago, J. Phys. D **36**, A249 (2003).

[25] M. Rauscher, R. Paniage, H. Metzger, Z. Kovats, J. Domke, J. Peisl, H.-D. Pfannes, J. Schulze, and I. Eisele, J. Appl. Phys. **86**, 6763 (1999).

[26] K. Shiraishi, Appl. Phys. Lett. **60**, 1363 (1992).

[27] B. K. Tanner, D. A. Allwood, and N. J. Mason, Mater. Sci. Eng., B **80**, 99 (2001).

[28] Y. Mizikawa, O. Komoda, and S. Miyase, Thin Solid Films **156**, 127 (1988).

[29] G. Hollinger, R. Skheyta-Kabbani, and M. Gendry, Phys. Rev. B **49**, 11 159 (1994).